



Phase diagram for two-dimensional layer of soft particles

Journal:	<i>Soft Matter</i>
Manuscript ID	SM-ART-02-2019-000333.R1
Article Type:	Paper
Date Submitted by the Author:	04-Apr-2019
Complete List of Authors:	Zhu, Xilan; University of Texas at Austin, McKetta Department of Chemical Engineering Truskett, Thomas; University of Texas at Austin, McKetta Department of Chemical Engineering and Department of Physics Bonnecaze, Roger; University of Texas at Austin, McKetta Department of Chemical Engineering and Texas Materials Institute



Journal Name

ARTICLE

Phase diagram for two-dimensional layer of soft particles

Xilan Zhu,^a Thomas M. Truskett^{a,b} and Roger T. Bonnecaze,^a

Received 00th January 20xx,
Accepted 00th January 20xx

DOI: 10.1039/x0xx00000x

www.rsc.org/

The phase diagram of a monolayer of soft particles described by the Daoud-Cotton model for star polymers is presented. Ground state calculations and Grand Canonical Monte Carlo simulations are used to determine the phase behavior as a function of the number of arms on the star and the areal coverage of the soft particles. The phase diagram exhibits rich behavior including reentrant melting and freezing and solid-solid transitions with triangular, stripe, honeycomb and kagome phases. These structures in 2D are analogous to the structures observed in 3D. The evolution of the structure factor with density is qualitatively similar to that measured in experiments for polymer grafted nanocrystals [Chen et al., *Macromolecules*, 2017, **50**, 9636].

Introduction

Underlying structure is the foundation to material properties. The prediction and control of structures at different length scales allows the engineering of properties and the design of functional materials. While structures with feature sizes on the order of 20 nm can be fabricated via top-down techniques such as photolithography¹⁻⁴ and imprint lithography^{5,6}, self-assembly of polymers and particles offers a path to make sub-20 nm or smaller structures⁷⁻¹⁰. Phase diagrams of these equilibrium self-assembled structures are important tools for the design of the components and processes to make the desired nanostructured materials. Here we are concerned with the phase diagram of three-dimensional (3D) soft particles confined to two-dimensions (2D), where the softness of the particles referred to here is determined by their pairwise interaction. Such particles suitably ordered on a surface can be used as a mask for patterning or directly as a functional component for the nano-enabled surface.

Because soft particles are deformable, their centers can be much closer than rigid particles of similar size. This leads to structures that cannot be achieved by equilibrium self-assembly of more rigid particles. Besides the commonly observed crystal structures of body-centered-cubic (BCC), face-centered-cubic (FCC), and hexagonal close packing (HCP)^{11,12}, novel crystals of diamond¹³, body-centered orthorhombic (BCO)^{13,14}, body-centered-tetragonal (BCT)^{13,15}, trigonal¹⁶, ellipsoidal phases (due to particle deformation)¹⁷ and polymorphic cluster phases¹⁸ have been identified for concentrated suspensions of

soft particles. Hertzian spheres have been shown to cycle among distinct crystal phases infinitely with increasing concentration¹⁴. Soft-particle interactions can also show unusual phase behaviours such as re-entrant melting^{13,14,18,19}. Phase diagrams of soft particles with external fields^{20,21} and shape anisotropy (e.g. patchy particles)²²⁻²⁴ have also been explored.

With the potential application of 2D crystals in electronic devices^{25,26} and optical devices²⁷, phase behaviour of soft particles in 2D is of interest. However, excluded volume effects and short ranged repulsion can cause jamming²⁸ of such particles and the self-assembly to dense, highly ordered monolayers can be problematic. Ultra-soft particle interactions can help achieve higher surface coverages and faster kinetics. Chen et al.²⁹ used ultra-soft polymer grafted nanocrystals (PGNCs) and showed self-assembled monolayer ordering in 2D via solvent annealing. The PGNCs—with their relatively small hard cores—can be modelled as star polymers, and their experimental phase behaviour exhibits similarities to that of the 3D phase diagram for star polymers¹³. Theoretical work has shown that the phase behaviour of soft particles in 2D is expected to be similarly complex^{30,31}, including a recent study using Hertzian spheres³².

Here we characterize the phase behaviour of ultra-soft 3D particles in a 2D monolayer. The Daoud-Cotton model for star polymers is used to describe the pairwise particle interactions. This interaction potential is simple and useful for understanding the self-assembly of nanoparticles that are grafted with polymers to impart stability in solution. It also allows direct comparison to experiments of Chen et al.²⁹. The resulting phases are set by the number of arms around each particle f and the areal density of the particles on the surface.

The remainder of the paper is organized as follows. Section 2 presents the pairwise interaction potential for the PGNCs, the

^a McKetta Department of Chemical Engineering, University of Texas at Austin, Austin, Texas 78712 USA

^b Department of Physics, University of Texas at Austin, Austin, Texas 78712 USA

† Footnotes relating to the title and/or authors should appear here.

Electronic Supplementary Information (ESI) available: [details of any supplementary information available should be included here]. See DOI: [10.1039/x0xx00000x](https://doi.org/10.1039/x0xx00000x)

numerical method used for the ground state calculation and the details for the Monte Carlo simulation. In section 3, we show the observed crystal structures and present a 2D phase diagram. In section 4, we compare the phase behaviour for the Daoud-Cotton model in 3D to 2D results. We then compare our predictions of structures to those experimentally observed by Chen et al. Finally, we summarize our findings in section 5.

Model and simulation details

Daoud-Cotton model

The PGNCs used by Chen et al. are composed of Fe_3O_4 nanocrystals grafted with polystyrene ligands. The PGNCs have a hard core surrounded by a soft region of polymers. The interparticle potential is chosen to be the Daoud-Cotton model^{29,33} for short-ranged interactions plus the addition by Likos and co-workers³⁴ of a Yukawa potential at longer distances. In the Daoud-Cotton model, each arm of a star polymer is described as a succession of spherical "blobs" whose size depends on r , where r is the distance from the center of the star. As described in Daoud-Cotton model, there are three distinct regions for each star polymer: the core (modelling the NC of PGNCs), and the unswollen and the swollen regions (modelling the grafted polymer strands emanating from the NC). The effective pair potential between star polymers is a combination of a stiffer logarithmic dependence inside the core ($r < \sigma$) and a softer Yukawa potential outside the core³⁴:

$$\frac{\Phi(r)}{k_B T} = \frac{5}{18} f^{\frac{3}{2}} \begin{cases} -\ln\left(\frac{r}{\sigma}\right) + \frac{1}{1+\sqrt{\frac{f}{2}}}, & r \leq \sigma \\ \frac{\sigma}{r} \frac{\exp\left[-\frac{\sqrt{f}(r-\sigma)}{2\sigma}\right]}{1+\sqrt{\frac{f}{2}}}, & r > \sigma \end{cases} \quad (1)$$

where the corona diameter σ describes the spatial extension of the monomer density around a single star and is defined as twice the distance from the center of the star to the center of the outermost blob. The pair potential in eqn. (1) is considered appropriate to represent PGNCs when those grafted polymer chains form a coating that effectively screens the core. It has also been used successfully for star-like micelles.³⁵⁻³⁸

As the pair potential given in Eq. (1) scales linearly with the thermal energy $k_B T = 1/\beta$, temperature T is not an interesting

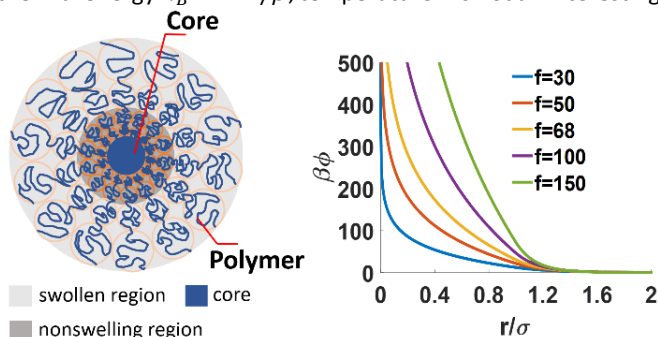


Figure 1 - Left: Sketch of a polymer grafted nanoparticle. Right: The Daoud-Cotton model pair potential as a function of the center-to-center separation r between two star polymers with various number of arms, $f = 30, 50, 68, 100$ and 150 .

thermodynamic parameter for the phase diagram of this model. The two-dimensional phase behaviour of this colloidal system depends only on the areal packing fraction $\eta = \pi\sigma^2 N/(4A)$, and the number of arms f grafted to a particle. In some key respects, the effect of f on the thermodynamic properties of this model is qualitatively similar to that of inverse temperature in atomic fluids.

Ground state calculation

For the Daoud-Cotton model in two dimensions, we carry out conventional ground-state calculations (described below) that determine the lowest energy states within a predetermined competitive pool of possible structures. We also carry out supplementary ground-state calculations using a genetic algorithm to test whether the lowest energy ground-state structures have indeed been included in the original competitive pool.

Optimization over competing structures

We carry out conventional ground state calculations that consider a finite number of competing crystal structures described in the Supplementary Information (SI). The average potential energy per particle u for particle crystals can be expressed as:

$$u = \frac{1}{2n} \sum_{i \neq j}^{r_{ij} < r_{cut}} \sum_{j=1,2,\dots,n} \Phi(r_{ij}) \quad (2)$$

Typical values of $f = 50, 68$ and 150 are used for the calculations. Here the potential energy is averaged over all particles within a single unit cell, equivalent to the average potential energy per particle over the entire system. n is the number of particles within a unit cell. r_{cut} is the cut-off distance. r_{ij} is the distance between the j th particle in the unit cell and the i th particle in the system. At zero-temperature, the chemical potential μ is equivalent to the enthalpy h and is given by:

$$h = u + pA \quad (3)$$

where A is the specific area and the system pressure p is given by the virial expression³⁹:

$$pA = -\frac{1}{4n} \sum_{i \neq j}^{r_{ij} < r_{cut}} \sum_{j=1,2,\dots,n} r_{ij} \Phi'(r_{ij}) \quad (4)$$

A search for the minimum h is performed using the interior point algorithm. To avoid being trapped in local minima and to ensure the globally optimal solution is obtained, the calculations are repeated with several initial conditions. The h - p curves for each competitor are used to identify the phase transition points and coexisting phases. We do not explore structures other than the ones mentioned in SI, since the ground state calculations reveal the same phases as the ones identified by a genetic algorithm and the Grand Canonical Monte Carlo simulations described below, indicating the initial pool of potential structures is adequate.

Genetic algorithms

Gottwald et al.^{40,41} has demonstrated the application of genetic algorithms (GAs) to successfully predict crystal structures at $T = 0$ in three dimensions⁴⁰. Here, we adapt their approach as a means to verify the ordered ground states predicted for the 2D Daoud-Cotton model by the aforementioned conventional method. Details of the implementation of the genetic algorithm are provided in the Supplementary Information.

The technique applied here finds the lattice structure that gives the lowest ground state energy u . The unit cell is represented by the primitive vector $\{\mathbf{x}_i\} = \{\mathbf{x}_1, \mathbf{x}_2\}$.

$$\begin{aligned} \mathbf{x}_1 &= a(1,0) \\ \mathbf{x}_2 &= a(x \cos \theta, x \sin \theta) \end{aligned} \quad (5)$$

where a is determined by the areal packing fraction of the system.

A large number of potential a 's are initially considered. Based on their fitness or lowest energy, the fittest structures survive and replicate. In the end, the fittest (or lowest energy) structure is identified.

Ground state calculations were initiated with 1000 random individual structures; crossover possibility $P_c = 0.1$ and mutation possibility $P_m = 0.05$ were adopted. All trials with $f = 50, 68, 150$ and packing fraction from 0.1 to 2.4 converged within 1000 generations.

Monte Carlo Simulation

We perform Grand Canonical Monte Carlo (GCMC) simulations to mimic the deposition process of particles in solution adsorbed onto a neutral substrate. Various packing fractions ($0.25 \leq \eta \leq 2.35$) and number of arms per particle ($30 \leq f \leq 150$) are simulated to provide information about the possible complex 2D phase behaviour of PGNCs. For each simulation, the chemical potential μ is specified, representing the fixed particle concentration from the reservoir. Similar to the method described in Ref. 28, the acceptance possibility P of each MC move (particle insertions, deletions, or translation) is determined by the change of potential ΔE .⁴²

$$P = \begin{cases} \min\left(1, \frac{A}{N+1} e^{-\beta\Delta E + \beta\mu}\right), & \text{insertions} \\ \min\left(1, e^{-\beta\Delta E}\right), & \text{moves} \\ \min\left(1, \frac{N}{A} e^{-\beta\Delta E - \beta\mu}\right), & \text{deletions} \end{cases} \quad (6)$$

A square simulation box with periodic boundaries is used. The simulation box is fixed in area A so that the number of particles N varies between 500 and 1000. The average number of particles and hence the packing fraction is dependent on μ . The corona radius $\sigma/2$ is considered to be the unit length. Approximately 5×10^7 Monte Carlo steps were used in each simulation. The system is expected to undergo two successive continuous transitions upon freezing (liquid to hexatic to triangular ordered phase) as predicted by Kosterlitz-Thouless-Halperin-Nelson-Young (KTHNY) theory. However, previous

work with similar soft particle models have shown that the hexatic region on the phase diagram can be extremely narrow^{32,40} and large-scale simulations are necessary for its characterization^{43,44}. Since our interests lie in exploring the various ordered 2D arrays that this model can assemble, we do not attempt to systematically probe the melting/freezing mechanism or to determine the boundaries of the hexatic phase.

Results

Figure 2 summarizes the predicted ground state phase diagram and gives a comparison between ground state structure and the equilibrium lattice structure by GCMC. At low η , the particles on the surface form a triangular phase. Within the triangular phase, all six neighbouring particles are separated by the same distance somewhere $r \geq \sigma$. Phase behaviour at higher packing fraction becomes richer as the particles interact more strongly, when $r < \sigma$. We identify four other crystal phases for $0.90 < \eta < 2.4$. A "stripe" phase arises at $\eta \sim 1.0$. This phase is an affinely-stretched triangular crystal. The first coordination shell lies inside σ and contains two particles. The second coordination shell sits at $r = \sigma$ and contains four particles. As the packing fraction increases further, more particles penetrate the corona and three more configurations are found to be ground state structures: the honeycomb phase, the kagome phase, and a second triangular phase. These phases give lattice structures with three, four and six particles within the first shell. Conventional ground-state calculations as well as GAs predict the same lattice structures. The coexisting regions have been identified between neighbouring phases. The ground state structures predicted by both methods and lattice parameters predicted by conventional calculation are given in SI. The ground state phases agree with the equilibrium phases simulated by GCMC.

Figure 3 shows the complete 2D phase diagram of particles with the star polymer potential constructed using the GCMC simulations. A fluid and several crystal phases are observed. The fluid phase is observed for $f < f_c \approx 33$ at all packing fractions. At least one stable crystal phase can be found above

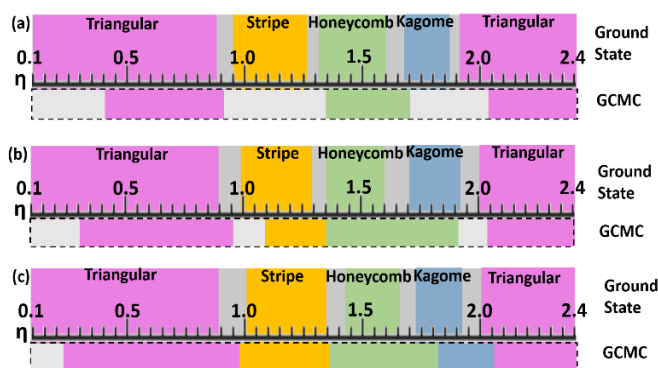


Figure 2 – Potential crystal structures determined by ground state calculation and GCMC. (a) $f = 50$, (b) $f = 68$ and (c) $f = 150$. Red: triangular; Yellow: stripe; Green: honeycomb; Blue: kagome; Grey: coexisting region (by conventional calculation) / fluid phase (by GCMC).

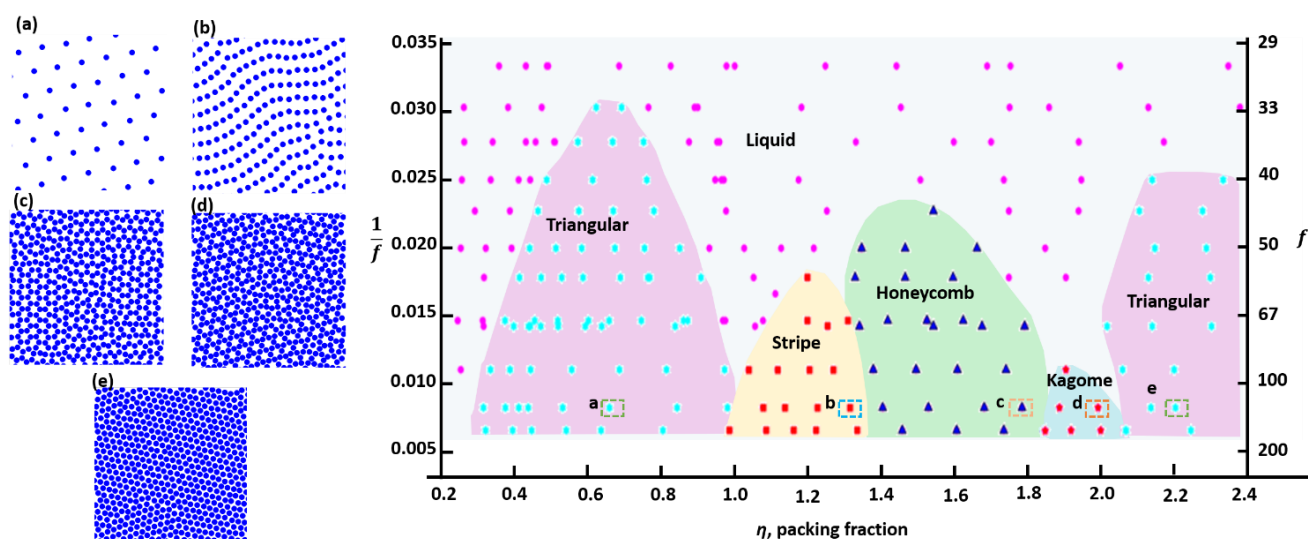


Figure 3 - Simulated 2D phase diagram for particles with the star polymer potential. (a)-(e) illustrate example structures for each solid phase at $f = 120$.

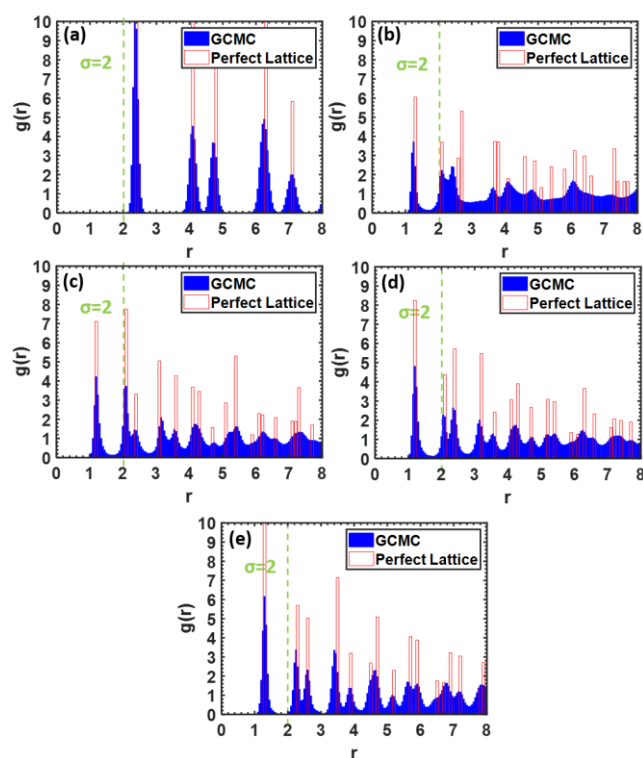


Figure 4 - Radial distribution functions of structures from GCMC simulations (blue) for each solid phase assuming perfect lattices at the same packing fraction: (a) triangular lattice, $\eta = 0.66$; (b) stripe lattice, $\eta = 1.31$; (c) honeycomb lattice, $\eta = 1.77$; (d) kagome lattice, $\eta = 1.98$; (e) triangular lattice, $\eta = 2.19$. All with $f = 120$. Green dashed lines indicate $r = \sigma$.

f_c . Reentrant melting and freezing are observed depending on the value of f for increasing packing fraction. For intermediate number of arms ($33 \leq f < 40$), reentrant melting occurs from the triangular phase to the liquid phase. Both reentrant melting and freezing can occur for $40 \leq f < 90$ with increasing packing fraction. For example, at $f = 50$, the structures transform from triangular to liquid to honeycomb to liquid to triangular as the packing fraction increases. For large f , as the system becomes

more densely packed, it goes through several solid-solid phase transitions. The solid phases observed in GCMC are consistent with the ground state calculation results, which progress from a triangular phase to stripe, honeycomb, kagome and a second triangular phase as the packing fraction increases. They are also analogous to structures reported for star polymers in 3D¹³.

To support the assignment of structures in the phase diagram, Figure 4 shows the radial distribution functions for each solid phase from the GCMC simulation and the radial distribution functions of structures assuming perfect lattices at the same packing fraction. For the first triangular phase, all peaks are located outside $r = \sigma$, showing no neighboring particles within the corona. For all other phases, we can see the first peak at $r = 0.65\sigma - 0.75\sigma$ and the second peak at $r = \sigma - 1.05\sigma$. As the system becomes denser, an increase in the first peak intensity within the corona diameter can be observed in Figure 4 (b)-(e). Because the effective temperature in the GCMC simulations is nonzero, we observed some expected spread in the particle position compared to the perfect crystal due to thermal oscillations, dislocations and grain boundaries.

Discussion

Jain et al. have demonstrated that ultrasoft isotropic interactions which stabilize a crystal structure in 3D may stabilize analogous structures in 2D⁴⁵. A comparison of our results with the 3D phase diagram¹³ may similarly help to understand the complex phase behaviour in 2D.

The transition to an ordered phase for this ultrasoft particle systems happens at a much lower η compared with hard spheres (i.e., $f \rightarrow \infty$). For hard spheres, the fluid phase is stable up to $\eta \approx 0.7$ and then the (two-step) transition to the triangular phase occurs⁴⁶. The triangular phase is stable up to the maximum packing fraction in 2D, $\eta \approx 0.91$. It is also observed in 3D that the system of ultrasoft particles freezes at

a small η compared to hard spheres. In this work, we did not explore extremely high arm numbers as the research in 3D has shown that hard sphere behaviour is not found for $f < 10000$. The extremely high f is also impractical to obtain in experiments.

The stable fluid phase within the range of $f < f_c \approx 33$ in our 2D results agrees with the 3D phase diagram ($f_c \approx 34$) reported by Watzlawek et al.¹³. At low packing fraction, all neighbouring particles have separations $r > \sigma$, and only the Yukawa portion of the pair potential comes into the play. In the 3D system, bcc/fcc phases were found at low packing fraction, $0.2 < \eta_{3D} < 0.7$. This is analogous to the phase behavior for charged colloids, whose interparticle interaction can be modelled by the Yukawa potential⁴⁷. The 2D phase transition from liquid to a triangular phase shows up as what is expected for a two-dimensional Yukawa system^{48,49}. With an increased packing fraction ($0.7 < \eta_{3D} < 1.5$), the reentrant melting and reentrant freezing transitions observed here were also reported for the 3D system at intermediate f ($34 < f < 60$). At higher f , two solid-solid phase transitions take place in the 3D system, first into a body-centered-orthogonal (bco) phase and then into a diamond phase. Analogous to the bco phase, a stripe phase is identified here in 2D. A similar stripe phase was observed by Malescio et al.⁵⁰ with purely repulsive isotropic pair potentials with two characteristic length scales. Anisotropy of the stripe/bco phase for our system can be explained similarly. For each particle in a dense cell, the overlap can happen in two ways: its corona overlapping with corona of all nearest neighbours, as opposed to being brought close with some neighbouring particles in one direction but with no corona overlap with all remaining particles. Given the weak divergence at small r and rapid drop at $r > \sigma$ for the star polymer potential, the second configuration yields the lower energy structure. Particles in either stripe or bco phases have two nearest neighbours at some distance within the corona. These two phases remain stable until the energy penalty of bringing nearest neighbours closer become significant and more particles cross over at $r = \sigma$. The next stable structures are two analogous crystals: a diamond phase in 3D and a honeycomb phase in 2D. The kagome/second triangular phases in two-dimensional systems at higher packing fraction can be explained by the corona overlap with a fourth/sixth neighbouring particle. The increased number of neighbouring particles within the corona is characterized by an increased first peak intensity in the radial distribution function. Similar to what has been stated for 3D¹³, many body interactions (ignored here) can be important for the actual star polymer systems for $\eta > 2\eta^*$, where η^* is the overlapping packing fraction $\eta^* = \pi/4$. At $\eta > 1.57$, three or more particles would be overlapping. Only pairwise interactions are considered in the model considered here. Since, for triplets, the multibody interaction in explicit star polymers was found to be attractive and small compared to the pairwise interaction⁵¹, we expect our predictions for experiments to be valid for packing fractions as high as those consistent with the honeycomb phase with three particles in the corona.

We turn now to a comparison of our theoretical predictions to the experimental observations made by Chen et al.²⁹. In the experiments, two different PGNCs with $f = 50$ and $f = 68$ were synthesized. The PGNCs have a hard-core diameter of 3.9 nm ($f = 50$) or 4.2 nm ($f = 68$). The thickness of the unswollen region for $f = 68$ samples were estimated indirectly through the measurements of the solvent intake volume of both the polymer film and PGNC film. The estimation suggested that effective screening is achieved by $f = 68$ samples. No experimental data was available for $f = 50$ samples. The synthesized PGNCs were self-assembled to form a monolayer using the solvent annealing method. The circularly averaged structure factor $S(q)$ was then measured for the self-assembled samples. The phase transition was identified according to the Hansen–Verlet rule⁵² and the ratio, q_2/q_1 , of the wave vectors of the first and second peaks in $S(q)$.

A good estimation of σ is critical for the direct comparison between simulation and experimental results. As no direct measurements are available, it is difficult to assign an unambiguous value for σ . The best estimation of the radius of PGNCs with $f = 68$ is $R \approx 4.9$ nm in toluene. Details can be found in the Supplementary Information (SI). We plot the structure factor for both experimental and simulation results in Figure 5 to help estimate σ . The large $S(q)$ value and oscillations near $q = 0$ before the first peak for the simulated structures (Figure 5 (a) (c)) are due to the finite box size and periodic boundary conditions and are not seen in the experimental results. The structure factor plots of the simulated $f = 68$ cases are rescaled assuming $\sigma/2 = 4.9$ nm and given in Figure 5(c). The first peaks of $S(q)$ sit roughly at the same values of q with the experimental measurements (Figure 5(d)), which confirms our estimation of σ . A slightly smaller R is expected for $f = 50$ as the core size is smaller and the ligand density is lower. A

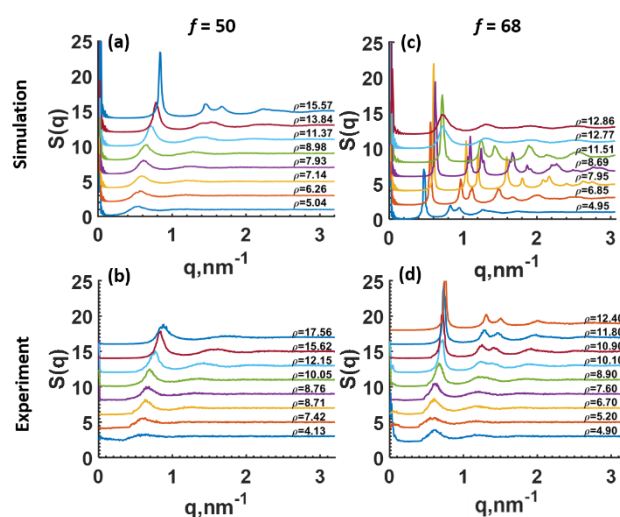


Figure 5 - Evolution of structure factor $S(q)$ for PGNCs with $f = 50$ (left column) or $f = 68$ (right column) from simulated structures (top row) and experimental results (bottom row). For the simulated results, the plots are rescaled assuming: (a) $\sigma/2 = 3.0$ nm; (c) $\sigma/2 = 4.9$ nm. (b), (d) experimental measurements reprinted from ref. 29 with permission. Number density (ρ) increases from bottom to top: (a) $5.04 \times 10^{-3} \text{ nm}^{-2}$ to $15.57 \times 10^{-3} \text{ nm}^{-2}$; (b) $\rho = 4.13 \times 10^{-3} \text{ nm}^{-2}$ to $17.56 \times 10^{-3} \text{ nm}^{-2}$; (c) $4.95 \times 10^{-3} \text{ nm}^{-2}$ to $12.86 \times 10^{-3} \text{ nm}^{-2}$; (d) $\rho = 4.90 \times 10^{-3} \text{ nm}^{-2}$ to $12.40 \times 10^{-3} \text{ nm}^{-2}$.

reasonable range would be $2.0 \text{ nm} < R < 4.9 \text{ nm}$. We rescaled the structure factor plots for the simulated $f = 50$ cases with several guesses of σ . The scattering vectors of peaks in $S(q)$ plot (Figure 5(a)) agree best with experimental measurements (Figure 5(b)) at $\sigma/2 = 3.0 \text{ nm}$.

For $f = 50$, no monolayer ordering was observed experimentally for $\rho \approx 4.1 \times 10^{-3} \text{ nm}^{-2}$ to $17.6 \times 10^{-3} \text{ nm}^{-2}$ ($\eta \approx 0.12 - 0.50$). However, the simulated data showed a split of the second peak in $S(q)$ (Figure 5(a)) at $\rho \approx 15.6 \times 10^{-3} \text{ nm}^{-2}$ ($\eta \approx 0.44$), and the ratio q_2/q_1 drops to $\sqrt{3}$. This indicates the appearance of triangular structure. For $f = 68$, the $S(q)$ plot of experimental data (Figure 5(d)) showed a split of the second peak and $q_2/q_1 \approx \sqrt{3}$ starting at $\rho \approx 10.1 \times 10^{-3} \text{ nm}^{-2}$ ($\eta \approx 0.76$). The simulation predicted the same transition at a lower density ($\rho \approx 5.0 \times 10^{-3} \text{ nm}^{-2}$ or $\eta \approx 0.37$). The experimental data are overlaid on the theoretical 2D phase diagram in Figure 6. In experiments a phase transition from liquid to hexatic phase is observed, which is similar to the first phase transition to triangular phase in the phase diagram. The phase diagram shows a possibility to achieve triangular ordering at a lower packing density than the experiments. No reentrant melting/freezing behaviour or transition to crystal phases other than triangular phase was observed yet in experiments as the packing density is low.

The differences between the experimental results and the theoretical prediction may arise for several reasons. The particle size comes from indirect measurements, which are done with the $f = 68$ sample. No experimental data are available for $f = 50$. The estimation of σ from the $S(q)$ fitting is inaccurate. The shifting of peaks in $S(q)$ is small when different values of $\sigma/2$ is used. Also, the star polymer size is concentration dependent⁵³ and can vary during the solvent evaporation/annealing process. A shrinkage in polymer size (estimated σ larger than actual) will cause the predicted phase to shift to higher η and span over a wider region than the actual equilibrium phase. A small deviation of σ can lead to a significant change of the predicted number density ρ where the phase transition happens (e.g. for $f = 68$, the phase transition happens around $\rho \approx 5.0 \times 10^{-3} \text{ nm}^{-2}$ if $\sigma/2 = 4.9 \text{ nm}$ and $\rho \approx 13.2 \times 10^{-3} \text{ nm}^{-2}$ if $\sigma/2 = 3.0 \text{ nm}$). Another possibility is that the polydispersity of PGNCs disrupts the ordering. The polydispersity of particles used in experiments is unknown. It has been shown that polydispersity can broaden the fluid phase⁵⁴, and the experiments will see less ordering than the theoretical prediction for monodispersed particles. Also, the nucleation of the star polymer system into a crystal can be difficult in experimental situations. The solvent annealing method pushes the system towards thermodynamic equilibrium. However, it is still possible that the self-assembly is diffusion limited. It has been found that the diffusion coefficient D in a star polymer system has a highly nonmonotonic behavior as a function of f and η .⁵⁵ The dynamics of the system can either be slowed down or increased with the increase of f and η . The absence of the predicted ordering in experimental results may indicate that the

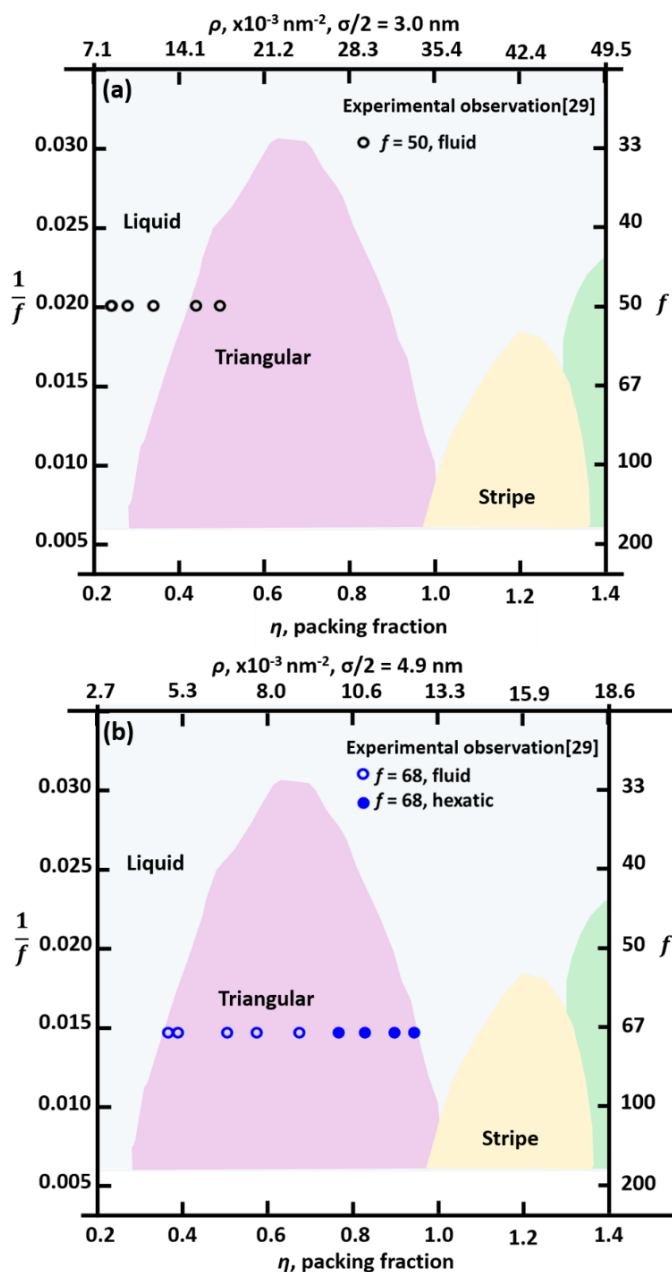


Figure 6 - Experimental self-assembly results from Chen et al.²⁹ overlaid on the crystal phases predicted by GCMC simulation. Experimental data rescaled assuming (a) $\sigma/2 = 3.0 \text{ nm}$ for $f = 50$, (b) $\sigma/2 = 4.9 \text{ nm}$ for $f = 68$.

system goes into disordered arrested states and the thermodynamic equilibrium is not reached.

The phase diagram is determined here for three-dimensional soft particles to two dimensions at equilibrium that can be described with pairwise potential given by eqn. (1). While this model is widely used for predicting the properties of symmetrically branched star polymers in 3D, it may not be accurate for PGNCs confined to a monolayer. As Che et al.⁵⁶ and Chremos et al.⁵⁷ have demonstrated, when the particles come close to the substrate, polymers interact with the substrate and the structural morphology of the soft particle is no longer identical to an isolated star polymer. The soft region of the particle deforms from the spherical shell to a polymer canopy.

The actual shape of soft particles is dependent on the surface energy of the substrate. Depending on the film thickness, the particles can also be confined at the air-liquid interface and deform accordingly. The exact calculation of the effective particle-particle interactions and particle-substrate interactions would require the modelling of polymer conformation under specific conditions (substrate surface energy, film thickness etc.). Coarse-grained models^{58,59} and self-consistent field theories^{58,60} have shown the capability to simulate single particle systems in such environments. Extending these approaches to develop models that incorporate such effects is an important area for future research.

Recently Bos et al.⁶¹ examined the effects of three two-dimensional pairwise potentials of star polymers. Each qualitatively followed the Daoud-Cotton model at short interparticle separations. At long distances the potential was either Gaussian, following the Yukawa potential, or vanished at a cut-off distance. It was found that the decay according to the Yukawa potential produced richer microstructures than the other two. Like the results presented in this paper, they found that the Yukawa potential produced triangular and honeycomb structures. Here more concentrated suspensions with greater numbers of arms were considered and so the phase diagram is broader. It also includes stripe and Kagome structures and re-entrant triangular lattice at large concentrations. Bos et al. observe the formation of two-dimensional crystals at lower values of f than observed here due to the differences between using a 2D versus a 3D potential.

Conclusion

Our calculations help to clarify the 2D phase diagram for ultra-soft particles as a function of the packing fraction η and the number of arms around each particle f , where the interparticle potentials are described by the Daoud-Cotton model with Likos correction for long ranged interaction. We identified several stable crystal structures at the ground state. The distinct crystal structures correspond to the triangular, stripe, honeycomb and kagome phases. We note some similarities between the phase diagrams in 2D and 3D. The critical value of f for the formation of stable crystals is $f_c \approx 33$, and a reentrant melting/freezing behaviour manifested at elevated f for both 2D and 3D cases. The crystal structures identified in 2D and 3D are analogous. The evolution of the structure factor of the model with particle density qualitatively agrees with that of experimentally studied polymer grafted nanoparticles.

Conflicts of interest

There are no conflicts to declare.

Acknowledgements

We thank R. Ruiz from Western Digital for sharing experimental data and fruitful discussions. This work was supported primarily by the National Science Foundation under Cooperative Agreement No. EEC-1160494. We acknowledge the Welch Foundation (F-1696) for partial support of this work. Any opinions, findings and conclusions or recommendations expressed in this material are those of the author(s) and do not necessarily reflect the views of the National Science Foundation or the Welch Foundation.

References

- H. Rodrigue, B. Bhandari, W. Wang and S.-H. Ahn, *Journal of Materials Processing Technology*, 2015, **217**, 302–309.
- M. Campbell, D. Sharp, M. Harrison, R. Denning and A. Turberfield, *Nature*, 2000, **404**, 53.
- L. Li, H. Lin, S. Qiao, Y. Zou, S. Danto, K. Richardson, J. D. Musgraves, N. Lu and J. Hu, *Nature Photonics*, 2014, **8**, 643.
- C.-J. Lee, H.-C. Yao, S.-L. Shue, T.-I. Bao and W. Yung-Hsu, *Method of double patterning lithography process using plurality of mandrels for integrated circuit applications*, 2017, US Patent 9,627,209.
- M. Caldorera-Moore, L. Glangchai, L. Shi and K. Roy, *UNE*, 2016, **13**, 15.
- K.-S. Han, J.-H. Shin, W.-Y. Yoon and H. Lee, *Solar Energy Materials and Solar Cells*, 2011, **95**, 288–291.
- M. A. Boles, M. Engel and D. V. Talapin, *Chemical Reviews*, 2016, **116**, 11220–11289.
- W. L. Xu, C. Fang, F. Zhou, Z. Song, Q. Liu, R. Qiao and M. Yu, *Nano Letters*, 2017, **17**, 2928–2933.
- J. P. Lagerwall, C. Schütz, M. Salajkova, J. Noh, J. H. Park, G. Scalia and L. Bergström, *NPG Asia Materials*, 2014, **6**, e80.
- C. F. Faul, *Accounts of Chemical Research*, 2014, **47**, 3428–3438.
- S. Auer and D. Frenkel, *Nature*, 2001, **409**, 1020.
- P. Pusey, W. Van Meegen, P. Bartlett, B. Ackerson, J. Rarity and S. Underwood, *Physical Review Letters*, 1989, **63**, 2753.
- M. Watzlawek, C. N. Likos and H. Löwen, *Physical Review Letters*, 1999, **82**, 5289.
- J. C. Pàmies, A. Cacciuto and D. Frenkel, *The Journal of Chemical Physics*, 2009, **131**, 044514.
- A. Yethiraj and A. van Blaaderen, *Nature*, 2003, **421**, 513.
- D. Gottwald, C. Likos, G. Kahl and H. Löwen, *Physical Review Letters*, 2004, **92**, 068301.
- V. M. Batista and M. A. Miller, *Physical Review Letters*, 2010, **105**, 088305.
- B. M. Mladek, D. Gottwald, G. Kahl, M. Neumann and C. N. Likos, *Physical Review Letters*, 2006, **96**, 045701.
- A. Lang, C. Likos, M. Watzlawek and H. Löwen, *Journal of Physics: Condensed Matter*, 2000, **12**, 5087.
- J. H. Schenkel, A. Samanta and B. J. Ravoo, *Advanced Materials*, 2014, **26**, 1076–1080.
- X. Xue, J. Wang and E. P. Furlani, *ACS Applied Materials & Interfaces*, 2015, **7**, 22515–22524.
- T. M. Hermans, M. A. Broeren, N. Gomopoulos, P. Van Der Schoot, M. H. Van Genderen, N. A. Sommerdijk, G. Fytas and E. Meijer, *Nature Nanotechnology*, 2009, **4**, 721.
- Z.-W. Li, Z.-Y. Lu, Z.-Y. Sun and L.-J. An, *Soft Matter*, 2012, **8**, 6693–6697.
- E. Bianchi, B. Capone, G. Kahl and C. N. Likos, *Faraday Discussions*, 2015, **181**, 123–138.
- D. Jena, K. Banerjee and G. H. Xing, *Nature Materials*, 2014, **13**, 1076.

- 26 C. Casiraghi and F. Withers, *2D Materials for Nanoelectronics*, 2016, **17**, 433.
- 27 Z. Sun, A. Martinez and F. Wang, *Nature Photonics*, 2016, **10**, nphoton–2016.
- 28 K. Schwenke and E. Del Gado, *Faraday Discussions*, 2015, **181**, 261–280.
- 29 J. Chen, A. Fasoli, J. D. Cushen, L. Wan and R. Ruiz, *Macromolecules*, 2017, **50**, 9636–9646.
- 30 W. L. Miller and A. Cacciuto, *Soft Matter*, 2011, **7**, 7552–7559.
- 31 S. Prestipino and F. Saija, *The Journal of Chemical Physics*, 2014, **141**, 184502.
- 32 Y. D. Fomin, E. Gaiduk, E. Tsiok and V. Ryzhov, *arXiv preprint arXiv:1801.10029*, 2018
- 33 M. Daoud and J. Cotton, *Journal de Physique*, 1982, **43**, 531–538.
- 34 C. Likos, H. Löwen, M. Watzlawek, B. Abbas, O. Jucknischke, J. Allgaier and D. Richter, *Physical Review Letters*, 1998, **80**, 4450.
- 35 B. Lonetti, M. Camargo, J. Stellbrink, C.N. Likos, E. Zaccarelli, L. Willner, P. Lindner and D. Richter *Physical Review Letters*, 2011, **106**, 228301.
- 36 S. Gupta, J. Stellbrink, E. Zaccarelli, C.N. Likos, M. Camargo, P. Holmqvist, J. Allgaier, L. Willner and D. Richter, *Physical Review Letters*, 2015, **115**, 128302.
- 37 S. Gupta, M. Camargo, J. Stellbrink, J. Allgaier, A. Radulescu, P. Lindner, E. Zaccarelli, C.N. Likos and D. Richter, *Nanoscale*, 2015, **7**, 13924.
- 38 M. Laurati, J. Stellbrink, R. Lund, L. Willner, E. Zaccarelli and D. Richter, *Physical Review E* 2007, **76**, 041503.
- 39 W. D. Piñeros, M. Baldea and T. M. Truskett, *The Journal of chemical physics*, 2016, **144**, 084502.
- 40 D. Gottwald, G. Kahl and C. N. Likos, *The Journal of Chemical Physics*, 2005, **122**, 204503.
- 41 T. Tüchtmantel, F. Lo Verso and C. N. Likos, *Molecular Physics*, 2009, **107**, 523–534.
- 42 M. P. Allen and D. J. Tildesley, *Computer simulation of liquids*, Oxford university press, 2017.
- 43 S. Prestipino, F. Saija and P. V. Giaquinta, *Physical Review Letters*, 2011, **106**, 235701.
- 44 K. Chen, T. Kaplan and M. Mostoller, *Physical Review Letters*, 1995, **74**, 4019
- 45 A. Jain, J. R. Errington and T. M. Truskett, *Physical Review X*, 2014, **4**, 031049.
- 46 A. Fortini and M. Dijkstra, *Journal of Physics: Condensed Matter*, 2006, **18**, L371.
- 47 H. Löwen and G. Krampposthuber, *EPL (Europhysics Letters)*, 1993, **23**, 673.
- 48 P. Hartmann, G. Kalman, Z. Donkó and K. Kutasi, *Physical Review E*, 2005, **72**, 026409.
- 49 H. Totsuji, C. Totsuji and K. Tsuruta, *Physical Review E*, 2001, **64**, 066402.
- 50 G. Malescio and G. Pellicane, *Nature Materials*, 2003, **2**, 97.
- 51 C. Von Ferber, A. Jusufi, C. Likos, H. Löwen and M. Watzlawek, *The European Physical Journal E*, 2000, **2**, 311–318.
- 52 J. Q. Broughton, G. H. Gilmer and J. D. Weeks, *Physical Review B*, 1982, **25**, 4651.
- 53 J. Stellbrink, B. Abbas, J. Allgaier, M. Monkenbusch, D. Richter, C. Likos, H. Löwen and M. Watzlawek, *Trends in Colloid and Interface Science XII*, Springer, 1998, pp. 25–28.
- 54 C. von Ferber, A. Jusufi, M. Watzlawek, C. N. Likos and H. Löwen, *Physical Review E*, 2000, **62**, 6949.
- 55 G. Foffi, F. Sciortino, P. Tartaglia, E. Zaccarelli, F. L. Verso, L. Reatto, K. Dawson and C. Likos, *Physical Review Letters*, 2003, **90**, 238301.
- 56 J. Che, K. Park, C. A. Grabowski, A. Jawaid, J. Kelley, H. Koerner and R. A. Vaia, *Macromolecules*, 2016, **49**, 1834–1847
- 57 A. Chremos, P. J. Camp, E. Glynos and V. Koutsos, *Soft Matter*, 2010, **6**, 1483–1493.
- 58 K. C. Daoulas, M. Müller, J. J. De Pablo, P. F. Nealey and G. D. Smith, *Soft Matter*, 2006, **2**, 573–583.
- 59 D. Marzi, C. N. Likos and B. Capone, *The Journal of chemical physics*, 2012, **137**, 014902
- 60 J. Paturej, A. Milchev, S. A. Egorov and K. Binder, *Soft Matter*, 2013, **9**, 10522–10531.
- 61 I. Bos, P. van der Scheer, W.G. Ellenbroek and J. Sprakel, *Soft Matter*, 2019, **15**, 615.